ADVANCED FUNCTIONAL MATERIALS
www.afm-journal.de

Tuning the Dielectric Properties of Individual Clay Nanosheets by Interlayer Composition: Toward Nano-Electret Materials

Sebastian Gödrich, Paul Markus, Matthias Stöter, Bernhard Biersack, Rainer Schobert, Josef Breu, and Georg Papastavrou**

To exploit the full potential of clays for electronic applications, a deeper understanding of how their dielectric properties can be tuned in a defined manner is essential. So far, most attention has been paid to the surface chemistry of clay platelets and their mechanical properties. Important properties, like electrical breakdown voltages, have been studied only on the macroscopic scale and not on the level of single platelets. One open important question that must be addressed is how far the dielectric properties, such as the breakdown characteristics, can be tuned by the composition of the interlayer. By using scanning probe techniques, it became possible to study individual platelets of the synthetic hectorite. Their interlayer composition is varied by encapsulating different cations between the silicate monolayers, besides sodium, ammonium, and an organic dye. The electrical breakdown characteristics of the monolayers and functional double stacks of hectorite are determined at the single platelet level. The use of these clay-based materials as electrets is evaluated by creating defined charge patterns at the nm-level and recording their isothermal potential decay. Thereby, the charge retention properties of the different clay compounds are determined.

1. Introduction

Clays are ubiquitous in nature and have been used as building materials in construction or pottery since the advent of civilization.[1,2] In particular, tablets made from clay were the first objects to preserve human writing in the form of cuneiform scripts.[3] In modern times, clay materials are widely used as fillers in innovative polymer composite materials[4–7] in order to modify and enhance the mechanical properties[8,9] or gas diffusion barriers for packaging materials.[10–12] Clay-based materials have also found applications in electronics. The first silicate used in this respect was muscovite mica, which up to this day is a very popular insulator in high-power circuits.[13,14] Currently, the insulation properties of related synthetic silicates are still of great interest[15–18] and novel composite materials for electrical applications are emerging.[19] It is known that silicate materials can be used as electrets,[20,21] which is a class of materials that can store a quasi-permanent electric charge[22,23] and are often referred to as space-charge electrets.[24] This effect allows for example for the construction of organic field effect transistors[25] and other electronic applications for 2D materials.[26,27] The polarizability of clays has been used in the past for electrostatic separation technologies, and pigments for surface coating and xerography have been reported.[28–30] It should be noted that clay-based electrets have also been used for energy harvesting applications.[31–34] Recently, clay materials have found applications in proof-of-concept studies, utilizing clay platelets as memory elements or transistors.[26,27,35–40]

So far, the dielectric properties of clays have received much less attention than their surface chemistry and mechanical properties, respectively.[2,41,42] Moreover, properties like dielectric constants or electrical breakdown voltages have been characterized primarily by macroscopic methods, while studies with nm-resolution have been reported only recently.[18,43–45] This study focuses on synthetic sodium fluorohectorite (Na^+-hectorite, $[Na_{0.5}]^{inter}[Mg_{2.5}Li_{0.5}]^{oct}[Si_4]^{tet}O_{10}F_2$), a 2:1 phyllosilicate that can be synthesized with enormous aspect ratios, in the order of 10.000–20.000, by osmotic delamination.[46,47] Na^+-hectorite belongs to a handful of layered compounds that show the rare

S. Gödrich, P. Markus, G. Papastavrou
Physical Chemistry II
University of Bayreuth
95440 Bayreuth, Germany
E-mail: georg.papastavrou@uni-bayreuth.de
B. Biersack, R. Schobert
Organic Chemistry I
University of Bayreuth
95440 Bayreuth, Germany
M. Stöter, J. Breu
Department of Chemistry
University of Bayreuth
95440 Bayreuth, Germany
E-mail: josef.breu@uni-bayreuth.de
J. Breu, G. Papastavrou
Bavarian Center for Battery Technology
University of Bayreuth
95440 Bayreuth, Germany

The ORCID identification number(s) for the author(s) of this article can be found under https://doi.org/10.1002/adfm.202509093

DOI: 10.1002/adfm.202509093

phenomenon of thermodynamically driven, spontaneous delamination via 1D dissolution.[48] They feature a superb homogeneous charge density, which allows for a sophisticated variation of the interlayer composition by a highly controlled cation exchange.[46,49] In particular, partial ion exchange can be directed toward heterostructures, where in a strictly alternating periodicity ordered interstratifications are produced of interlayers that are activated and deactivated toward 1D dissolution. When these heterostructures are immersed in water, every other interlayer is blocked from 1D dissolution. Consequently, instead of monolayers, double stacks are obtained, where two silicate monolayers are adhered together by a cation deactivating the 1D dissolution. Deactivating cations can be both inorganic cations of low hydration enthalpy[50] or hydrophobic organo-cations.[4,51] The synthesis of double stacks via the 1D dissolution of ordered heterostructures represents the most direct approach to alter the dielectric properties on the level of single nanosheets. To characterize thesesystematically varied dielectric properties in a systematic way, we will not utilize bulk measurements but rather address the dielectric properties on the level of individual clay nanosheets by adapting methods that are based on scanning probe techniques. These techniques have been primarily used for studying organic and inorganic thin films.[52,53] For example, silicon oxide as a common dielectric layer for semiconductor devices has been studied extensively[54–56] and recently, hexagonal boron nitride and transition-metal dichalcogenides (for example, MoS_2) have received increasing attention as emerging 2D-dielectrics.[39,57,58] However, comparable studies of the electronic properties of individual clay nanosheets are scarce to the best of our knowledge.[18] The main techniques used here were local conductivity measurements and charge injection by conductive atomic force microscopy (AFM) with a metallic cantilever tip.[59] This setup allows for locally capturing I–V curves, from which the breakdown voltages for individual clay platelets can be determined. Moreover, a slightly modified setup allowed us to generate defined charge patterns and high-resolution surface potential imaging of these patterns using Kelvin Probe Force Microscopy (KPFM). Furthermore, the combination of this technique with a heating stage allowed us to perform isothermal surface potential decay measurements, which is a standard procedure to study the relaxation mechanisms in electret materials. A similar approach for isothermal potential decay by AFM has been reported recently for organic electret materials.[60]

2. Results and Discussion

2.1. Synthesis and Characterization of the Hectorites

Ordered heterostructures were synthesized by partial ion exchange from pristine Na^+-hectorite.[47,49] The incoming cations require different gallery heights, both larger or smaller than hydrated Na^+: (NH_4^+)[50] facilitates smaller gallery heights (cf. **Figure** 1a) and (6-[3-(4-Nitrostyryl)-6-methoxyphenyloxy]-hexyl triethyl ammonium larger gallery heights than Na^+ (abbreviated as HEMONS) (cf. Figure 1b). Thus, both of these types of cations will segregate into different interlayers than the hydrated Na^+-interlayers. As a 1D periodic arrangement of the two types of interlayers is favored by the Madelung factor over a random arrangement, the segregation occurs, moreover, in a strictly alternating fashion. During ion exchange, the ionic strength is at a level where the 1D dissolution of all types of interlayers is impeded. Once the ionic strength is subsequently lowered by repeated washing, 1D dissolution eventually sets in but is restricted to the Na^+ interlayers. The heterostructures delaminate strictly into double stacks, where NH_4^+ and HEMONS$^+$ cations are sandwiched between two anionic silicate monolayers. We refer to these nanosheets in the following as NH_4^+-double stacks (cf. Figure 1a) and HEMONS$^+$-double stacks (cf. Figure 1b), respectively. While NH_4^+ approximates a spherical electron density, the bulky organo-cation was chosen for its large dipole moment. The schematic representations for the double stacks of both types are shown in Figure 1. The external basal planes of these double stacks carry appropriate amounts of Na^+ to assure charge balance while assuring the electrostatic stabilization of the aqueous dispersions. The aqueous suspensions of individual, delaminated double stacks and for comparison Na^+-nanosheets, respectively, were drop-casted onto ultra-flat template-stripped gold substrates and studied by various AFM-based nano-electrical characterization methods.

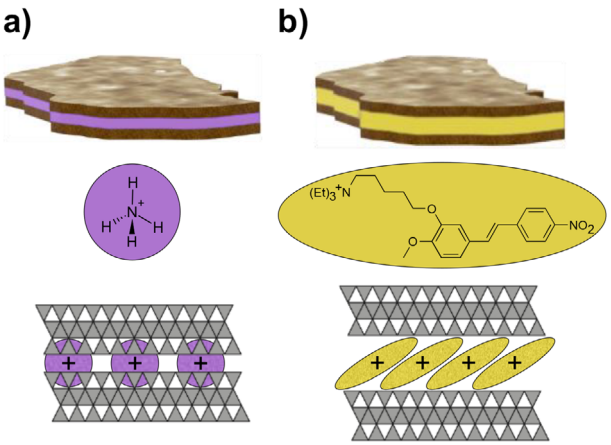

Figure 1. Schematic representation of the two types of double-stacks studied: a) NH_4^+-double stacks and b) HEMONS$^+$-double stacks.

A flat and homogeneous topography is typical for Na^+-nanosheets when deposited onto a substrate with sufficiently low roughness.[61,62] Monolayer Na^+-nanosheets (as shown in **Figure** 2a) have typical lateral dimensions in the range of several micrometers and an apparent thickness of ≈1.4 ± 0.2 nm under ambient conditions (cf. **Table** 1). The heights of the bi– and trilayers are larger but not multiples of the height of a single Na^+-nanosheet (cf. Table 1). The bi- and trilayers result from an incomplete delamination down to the level of single nanosheets and have not been prepared specifically but can be found after deposition of the monolayers on the substrates as well. All of our experiments were performed in a humidity range, where the sodium interlayers occur in a hydrated state.[47] Therefore, the measured heights of the monolayer samples (1.4 ± 0.2 nm) are larger than expected for an individual hectorite nanosheet (≈1.0 nm).[63] On the contrary, the NH_4^+-occupied interlayers in NH_4^+-double stacks do not hydrate; thus, their sample thickness of 2.1 ± 0.3 nm is even smaller than the one observed for the bilayers of Na^+-hectorite (2.7 ± 0.3 nm). The heights measured for the HEMONS$^+$-double stacks are in-line with previously reported

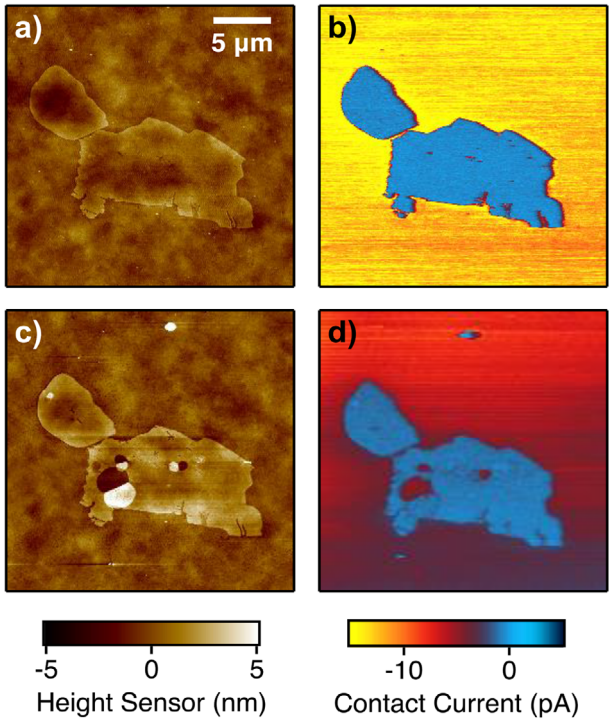

Figure 2. Conductive AFM measurements of Na^+-hectorite monolayers on template-stripped Au-substrates. a) Topography image of a nanosheet and b) corresponding current image showing the insulating properties of this nanosheet. c) Height and d) current images of the same nanosheet after several I–V measurements.

structural data for intercalated molecules with dimensions comparable to HEMONS.[51,64]

2.2. Electrical Breakdown Experiments

The electrical characterization of the different nanosheets was performed by conductive AFM along with cantilevers made from platinum (Pt) wire. Such solid metal cantilevers provide the robustness to perform multiple electrical breakdown experiments whilst maintaining a conductive apex. The samples were immobilized on ultra-flat, conductive gold (Au) substrates. Van-der-Waals forces provided sufficient attraction for permanent immobilization. Before conducting the breakdown experiments, the topography of the individual nanosheets was determined by imaging via Peak Force tapping under ambient conditions (cf. Figure 2a). During AFM-imaging, a small DC voltage was applied between the Au-substrate and the conductive cantilever, and the current flowing at the tip-sample contact was recorded as a function of the lateral positions on the basal surface of the nanosheets. The insulation properties of the single Na^+-hectorite nanosheets yield a strong contrast to the underlying highly conductive gold substrate (Figure 2b). Small defects in the nanosheet morphology, which could hardly be seen in the height image, were revealed as small conductive areas. Such defects are a relatively common feature. Analogous measurements were carried out for NH_4^+-double stacks and $HEMONS^+$-double stacks.

The analysis of the electrical insulation and breakdown behavior was conducted by current vs. voltage measurements, in the following referred to as I–V curves. For these experiments, the cantilever was positioned at a specific location on top of the different types of nanosheets. The large aspect ratios of $\gtrsim$5.000,[46,47] allowed for the exclusion of border effects. Then, linear voltage ramps were applied while acquiring the current flowing between the conductive Au-substrate and the solid Pt-cantilever, which are both sandwiching the nanosheets. The measurements were performed not at borders of the nanosheets in order to prevent gaseous breakdown via the gold substrate. The resulting I–V curves will be discussed later. After the acquisition of several I–V curves, the same single Na^+-hectorite nanosheet was imaged for *post-mortem* analysis (cf. Figure 2c). We observed that during the I–V measurements of the hectorite samples, small circular fragments were often cut out from the platelet, exposing the underlying substrate (Figure 2c). The fragments often remained attached to the main nanosheet on one side, mimicking an open door. The complete detachment from the substrate was demonstrated by the contact current images, where high conductivity was observed in these areas (Figure 2d). This effect was frequently observed not only for the Na^+-hectorite nanosheets but also for the two types of double-stacks. Exemplary AFM images of a $HEMONS^+$-double stack featuring the same effect are shown in Figure S1 (Supporting Information). Various breakdown mechanisms contribute to the reported dielectric and electro-mechanical breakdown.[23] These contributions cannot be clearly separated on this scale. The electro-mechanical stress on the nanosheet as an intermediate dielectric is supposed to be extremely large due to the high electric field strengths. In consequence, large electro-mechanical forces could act. Along with pre-existing small defects in the nanosheets, a local breakup due to the mechanical stress by the external electrical fields with a "punch-effect" has been observed before.[65] Moreover, the low-density domains of the ionized material may have been trapped beneath the platelet by impact ionization during the charging process.[66] This volatile material might depressurize by the concentric destruction of the overlaying nanosheet.

Table 1. Height and electrical properties of all examined nanosheet types.

	Nanosheet Height h [nm]	Positive Breakdown Voltage U_B^+ [V]	Breakdown Asymmetry ΔU_B [V]	Dielectric Strength E_{max} [MV cm^{-1}]
Na^+-hectorite Monolayer	1.43 ± 0.23	4.10 ± 0.30	0.93 ± 0.29	25.2 ± 5.5
Na^+-hectorite Bi-Layer	2.72 ± 0.26	6.16 ± 0.45	1.29 ± 0.38	20.3 ± 3.4
Na^+-hectorite Tri-Layer	3.90 ± 0.30	7.20	n. a.	16.3 ± 1.9
NH_4^+-Double Stack	2.09 ± 0.25	5.70 ± 0.24	0.80 ± 0.35	25.3 ± 4.0
$HEMONS^+$- Double Stack	2.73 ± 0.26	5.34 ± 0.24	−0.08 ± 0.23	19.7 ± 2.1

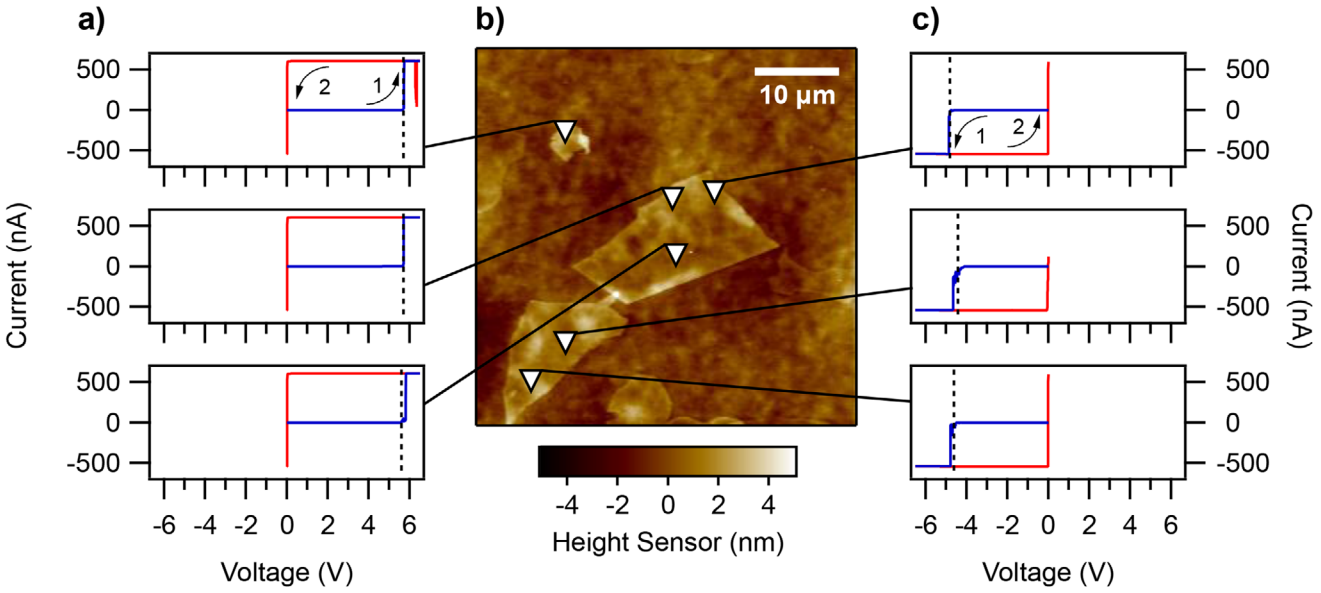

Figure 3. I–V measurements on different spots of three individual NH_4^+-double stacks, as indicated on the topography image (b). a) I–V-curves for positive potential ramps and c) negative potential ramps. The dashed lines indicate the respective breakdown voltages.

Figure 3 shows typical I–V ramping experiments for NH_4^+-double stacks. Analogous examples for HEMONS$^+$-double stacks are given in the Supporting Information (cf. Figure S2, Supporting Information). For every sample, various spots on different double stacks were selected for acquiring the I–V curves (Figure 3b). After positioning the cantilever guided by the topographic image acquired first, the voltage was swept in a range of 0 to ±10 V and back to detect the electrical breakdown. During these electrical measurements, a constant force of the order of 1 µN has been applied. Either positive or negative voltage ramps have been executed. Figure 3a shows three exemplary I–V curves for both polarities. Initially, no current flow was detected, while the voltage magnitude continuously increased until a sudden electrical breakdown of the double-stack nanosheets took place (blue curves). The electrical breakdown event can be clearly attributed to a practically instantaneous transition from an insulating to a highly conductive state. After the dielectric breakdown, the electrical current was limited to ±600 nA, which corresponds to the saturation value for the current amplifier connected to the AFM. Reversing the voltage ramp after the breakdown (red curve) leads to a constant current flow in the saturation regime of the amplifier.

The I–V curves acquired for the positive and negative potential ramps show very different breakdown voltages, as shown in an exemplary manner in Figure 3a (positive ramp) and Figure 3c (negative ramp), respectively. For the positive ramps, the average breakdown voltage for NH_4^+-double stacks was +5.70 ± 0.24 V. For the negative ramps, a breakdown voltage of −4.87 ± 0.31 V was measured, which was significantly lower in magnitude. This breakdown asymmetry was also detected on different spots of the same double stack and therefore cannot be attributed to local differences in height or composition.

The electrical breakdown characteristics were studied for the mono-, bi-, and trilayers of the Na^+-nanosheets as well as both types of double stacks in an analogous manner to Figure 3. Exemplary measurements for HEMONS$^+$-double stacks as well as the Na^+-hectorite mono- and bilayers are shown in cf. Figures S2 and S3 (Supporting Information). The averaged breakdown voltages for the positive voltage ramps have been compiled in Table 1. Depending on the type of cation sandwiched in the double stacks, small differences in the average breakdown voltages were observed. Hence, as expected, the nature of the interlayer plays a role in the electrical properties: In-line with general expectations, the bulkier HEMONS$^+$ leads to a larger spacing between the two silicate monolayers, resulting in a slightly higher average breakdown voltage compared to the smaller NH_4^+ interlayer. In the same line of argumentation, for the Na^+-hectorite nanosheet bi- and tri-layers, which also display larger heights than NH_4^+-double stacks, the average breakdown voltage also increased with the overall thickness of the dielectric layer.

The compilation of data in Table 1 illustrates that for the Na^+-hectorite monolayers and NH_4^+-double stacks, the breakdown voltages were not identical in magnitude for the positive and negative ramps. The difference in magnitudes is expressed by $\triangle U_B$. The full dataset has been compiled in cf. Table S1 (Supporting Information). For the Na^+-hectorite monolayers and NH_4^+-double stacks, distinctly higher breakdown voltages were observed at positive potentials. The dielectric breakdown process is supposed to be initiated by the charge carrier injection from one electrode.[66] In this case, the initial emission of a hot electron into the dielectric will strongly depend on the involved energy levels. In our experimental setup, two different metals, namely Pt (AFM-tip) and Au (substrate electrode), were used for contacting the dielectric, i.e., the nanosheets. The resulting non-neutral electrode configuration leads to an intrinsic distortion of the energy levels that could affect the breakdown voltage measurement. However, any electric field enhancement due to the electrode shape is neglected in this study. Interestingly, the HEMONS$^+$-double stack samples did not show a difference in the breakdown voltage for the different polarities (cf. $\triangle U_B$ in Table 1). This

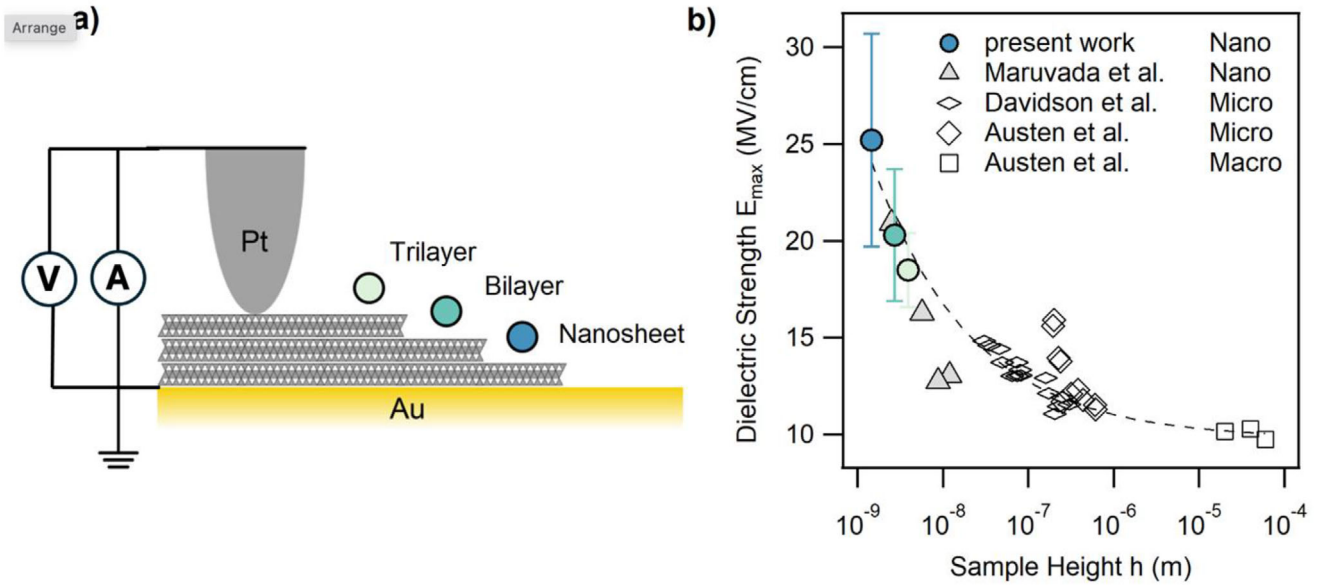

Figure 4. a) Schematic representation of the measurement setup for dielectric breakdown measurements of nanosheets. b) The dielectric strength of layered silicates for various specimen thicknesses. Micro- and macroscale measurements on muscovite mica, as reported by Maruvada et al.[43] (triangles), Austen and Whitehead[72] (squares), as well as Davidson and Yoffe[73] (rhombs). These data are in-line with the nano dielectric measurements (circles) of this study. The dashed line represents a guide to the eye.

observation cannot be directly related to the electrode separation as we observed asymmetric, albeit higher, breakdown voltages $U_B{}^+$ for the Na^+-hectorite bilayers. A possible explanation might be related to the size, shape, and conjugated nature of the organization in the interlayer, which might lead to an electrically conducting interlayer gap.

By determining the nanosheet height as well as the breakdown voltage, all parameters were available to estimate the dielectric strength on the level of individual nanosheets.[58,67] The dielectric strength is defined as the maximum electric field that an insulator can withstand before an electrical discharge occurs through the material. For macroscopic samples, the dielectric strength is commonly obtained by dividing the measured breakdown voltage by the sample thickness.[68,69] A sphere-plane electrode geometry is the recommended electrode configuration for insulation testing according to the cited standard procedures, which is comparable to the configuration of an AFM-tip and a flat electrode. However, the required specimen thickness of 1.0–3.2 mm[68,69] is 6 orders of magnitude larger than that in the nanosheet experiments. The resulting dielectric strength E_{max} for the different types of nanosheets has been compiled in Table 1. The highest dielectric strengths were observed for Na^+-hectorite monolayers and $NH_4{}^+$-double stacks.

For macroscopic samples, the dielectric strength is supposed to be independent of the sample thickness.[68,69] However, for very thin specimens whose thickness is in the order of a few mean free path lengths, which corresponds to 0.5–2 nm for solids,[66] the dielectric strength increases with decreasing thickness.[70] This relation was first theoretically postulated by Fröhlich and Mott.[71] Austen and Whitehead observed a similar effect for the electrical breakdown of muscovite mica, which is a phyllosilicate model system, with the same 2:1-layered structure but a different composition of the layers and non-hydrated K^+-interlayers as compared to the herein used hectorite.[72] Later, Davidson et al. recorded breakdown measurements that corrected and extended the studied thickness range down to 20 nm for mica.[73] In our study, the range of the sample thickness was extended to the smallest possible range, namely down to individual Na^+-nanosheets with a controlled and defined thickness of <5 nm. **Figure 4a** illustrates the measurement setup for the individual nanosheets (as well as bi- and tri-layers) schematically. Figure 4b shows the dielectric strength derived for 1–3 layers of Na^+-nanosheets in comparison to the values reported for mica samples of various thickness.[72,73] The specimen thickness in Figure 4b covers about five orders of magnitude. The here-determined values for the a nanosheet monolayers as well as the bi- and trilayers fall nicely in the trend outlined by the previously reported mica data.[72,73] In particular, we find a good match with the data reported by Marudvada et al., which have been acquired as well by an AFM-based approach.[43]

Similar to the K^+-interlayer cations in micas, $NH_4{}^+$-interlayer cations are known to protrude into the upper and lower hexagonal cavities of the silicate surface, creating a dense crystalline structure in the interlayer (cf. Figure 1a).[50] Therefore, the measured dielectric strength of $NH_4{}^+$-double stacks (25.3 ± 4.0 MV cm^{-1}) is similar to the dielectric strength of an individual monolayer (25.2 ± 5.5 MV cm^{-1}). The reduced dielectric strength of $HEMONS^+$-double stacks results most likely from the intercalated conjugated organocations. Fröhlich postulated that the dielectric strength of a mixed crystal approaches the weighted mean of those of the pure substances.[74] Following this argumentation, the loss of dielectric strength in the $HEMONS^+$-double stacks results from the reduced dielectric strength of the organic interlayer. Dielectric strengths of <8 MV cm^{-1} have been reported for organic self-assembled monolayers (SAMs), which are practically

independent of their molecular structure.[75,76] The dielectric properties of the densely-packed organization interlayer can be approximated by those of a SAM. The resulting weighted average (2:1 ratio of E_{max}[hectorite monolayer] ≈25 MV cm^{-1} and E_{max}[SAM] ≈8 MV cm^{-1}) provides 19.3 MV cm^{-1}, which is a surprisingly good first approximation for the observed reduced dielectric strength of 19.7 ± 2.1 MV cm^{-1} (cf. Table 1). Accordingly, the reduced dielectric strength of the restacked bi- and trilayers of Na^+-hectorite must be attributed to the influence of the same hydration layers that are already responsible for the difference in the observed heights. The relevance of interlayer water for breakdown investigations has been reported previously.[77] The presence of confined water layers is expected for the here-studied hectorite nanosheets as well as for the multilayers.[78] Water also plays an important role in the electro-mechanical and thus electrical breakdown, especially due to thermal effects.[79] It should be pointed out that the here determined values for the E_{max} are in the same order of magnitude as the ones reported for a 3 nm-thick layer of hexagonal boron nitride, which is one of the few comparable studies available considering the height range of the nanosheets.[58,67]

2.3. Clay Nanosheets as Electret Materials

Electrets are materials that can store electric charges, which is an effect that has also been reported for silicates, such as mica.[20,21] However, the double stacks studied here should also be perceptible to the polarization of their interlayers and thus provide a different polarizability than the monolayers or stacks of those. In order to follow the underlying process, we utilized again measurement techniques based on scanning probe techniques: Defined charge distributions can be imprinted or 'written' in the double stacks by means of conductive AFM using the same configuration as for the breakdown voltage measurements. The resulting charge pattern can be imaged by scanning Kelvin Probe Force Microscopy (KPFM).[80] **Figure 5** shows schematically how the 'writing' and 'reading' of charge patterns was implemented here. The procedure utilized here is analogous to the one recently reported by us for organic electret materials.[60] Similar experiments have been reported for inorganic dielectrics.[81,82] Suitable nanosheets have been identified first by imaging in contact mode under ambient conditions. The charge patterns have been 'written' while scanning a predefined vector path and applying a constant charging voltage of +3 V to the tip. This potential remains significantly below the predetermined breakdown voltages. As an homage to the first recordings of human writing, we chose a vector path forming a cuneiform script ('*IM*' which means clay, loam in old Sumerian,[83] cf. **Figure 6c**). Early writing was typically imprinted and preserved on macroscopic clay tiles, which before firing were composed of nanoscopic clay platelets like the well-defined clay nanosheets applied in this study.

The resulting charge patterns were imaged by Kelvin Probe Force Microscopy (KPFM) as illustrated in Figure 5b. Here, KPFM-imaging was carried out by the so-called dual-pass amplitude modulation technique;[80] In the first scan, the topography is determined. Subsequently, in the second re-scan, the cantilever is lifted by a predetermined lift height from the surface (here: 30 nm) and follows the sample topography of the previous scan

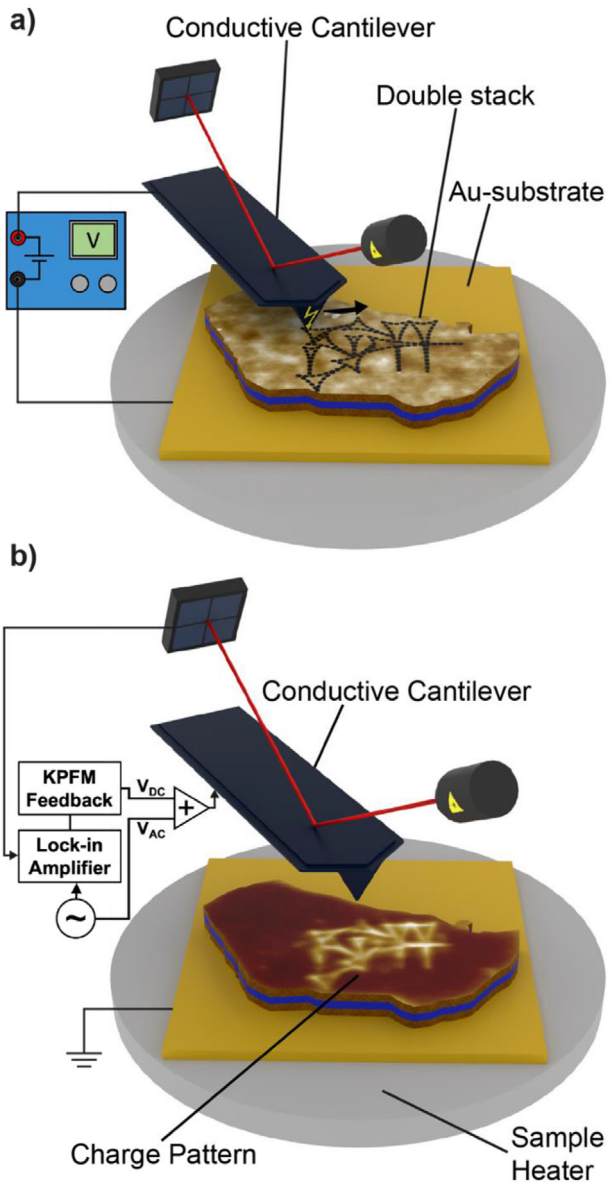

Figure 5. a) Scheme of the AFM-based local charging process: A conductive AFM tip is brought into contact with a clay nanosheet lying on a gold substrate. During charging, the tip is scanned along the predefined vector path with an applied DC voltage contact mode. b) For the read-out, the AFM tip is withdrawn from the surface, and Kelvin Probe Force Microscopy (KPFM) is used to read-out the generated charge patterns. Optionally, the sample can be heated with a sample heater during the read-out to accelerate the charge decay.

at this distance. During this lift scan, the mechanical excitation of the cantilever is switched off and an AC voltage is applied to the conductive cantilever. This AC-signal is modulated with an additional DC voltage that is controlled by a feedback loop to nullify the resulting cantilever oscillation. The latter DC-signal corresponds to the local surface potential on the sample.[80]

Figure 6 shows a proof-of-principle for the controlled charging of an individual NH_4^+-double stack. The topographic image and the surface potential distribution were determined by KPFM,

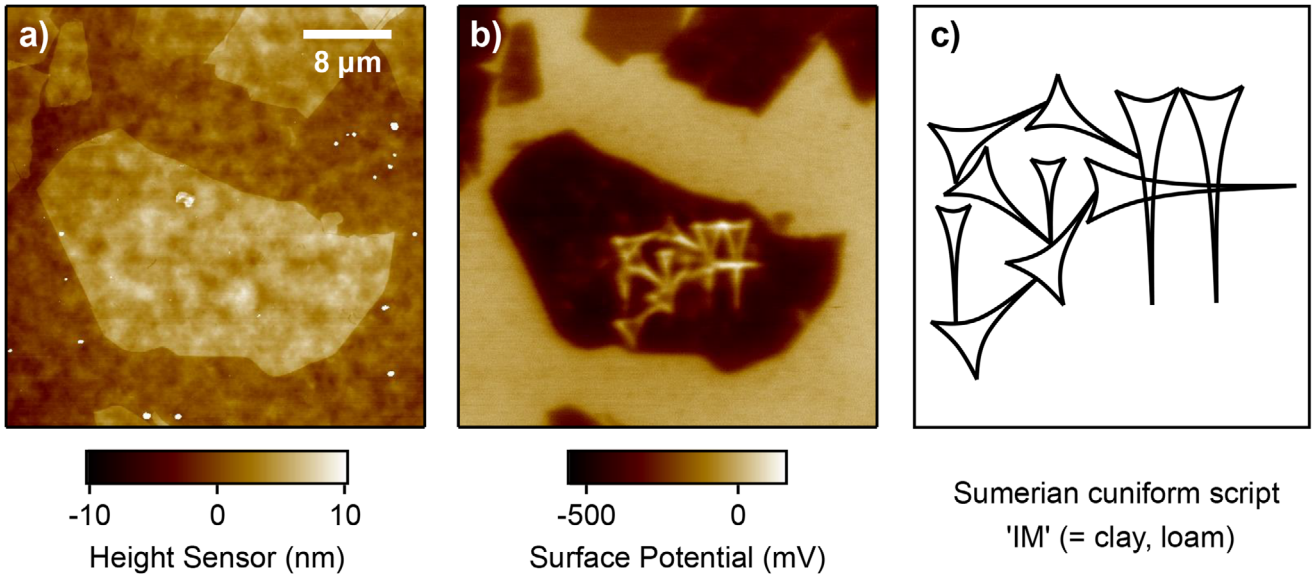

Figure 6. a) AFM topography image after contact charging NH_4^+-double stacks. b) Corresponding KPFM surface potential image (relative to gold) of a selectively charged 30 µm wide double stack showing the term IM (= clay, loam) in Sumerian cuneiform script. c) Vector graphics used to write the Sumerian cuneiform script pattern with +3 V charging voltage.

as shown in Figure 6a,b, respectively. Figure 6c shows the original vector path that has been written in the NH_4^+-double stack. The cuneiform symbol is clearly visible on the surface potential map. However, the topography of the double stack remains unchanged after the charging procedure, as confirmed by the topography image of the nanosheet after charging (cf. Figure 6a). Possible mechanisms for the charging of hectorite nanosheets have been discussed in literature[84,85]: Local destruction, reduction or oxidation of the dielectric[84] can be ruled out as the sample topography remains unaffected by the charging process (cf. Figure 6a). Therefore, we assume that an electret-like charge-carrier injection mechanism facilitates the charge patterning of the double stacks.[22] The charge patterns are stable at room temperature and under ambient conditions. Based on Figure 6, we estimate that a resolution of <250 nm has been achieved for the charge patterning.

2.4. Isothermal Potential Decay for Charges Stored in Double Stacks

Isothermal potential decay (ITPD) is a standard technique for characterizing macroscopic electret samples.[23] We transferred the ITPD approach to the AFM in order to achieve locally resolved ITPD-measurements at the nm-level.[60] This technique is also well-suited to study the charge decay on individual hectorite nanosheets. Due to the restricted space on the platelets, square-shaped charge patterns were written into the double stacks with potentials of either +3 V or −3 V. Subsequently, the nanosheet's topography and surface potential were measured by KPFM-imaging at room temperature. To accelerate the charge decay, the samples were then heated to 70 °C using a sample heater stage during consecutive KPFM-measurements (cf. Figure 5b). **Figure** 7a,b show the topography and surface potential images of the charged $HEMONS^+$-double stacks. The potential map reveals inhomogeneities within the surface potential distribution of the individual nanosheets (cf. white squares, Figure 7b). Analogous charge patterns were also written in NH_4^+-double-stacks samples (Figure 7e,f). The regions of two separate double stacks in the upper image area were charged positively, and another two in the lower image area were charged negatively, resulting in white and black squares, respectively. Compared to the NH_4^+-double stacks, the patterns are less well-defined at the edges for the $HEMONS^+$-double stacks. It should be pointed out that the interlayer of $HEMONS^+$ is formed by molecules with a much larger dipole moment than for NH_4^+. Hence, not only the lateral structure of the charge patterns should show differences but also the potential decay upon thermal treatment.

To quantify the potential decay with increasing annealing time, the KPFM signal was averaged for each square along the slow scan axis within the inner 60% of the written charge pattern on a double stack (cf. dashed boxes in Figure 7b). These averaged cross-sections are exemplarily shown in Figure 7c for different annealing times with positive and in Figure 7d with negative charging potentials, respectively. Figure 7g shows the decay in the surface potential as a function of time for both types of double stacks. The surface potential values were normalized to the initial surface potential after charging and plotted as a function of time (Figure 7g). A more detailed analysis of the surface potential decay for NH_4^+-double stacks, $HEMONS^+$-double stacks, and Na^+-hectorite monolayers can be found in cf. Figures S4–S6 (Supporting Information). The surface potential decays exponentially with time, regardless of whether a nanosheet has been positively or negatively charged. A similar behavior has been observed for pure organic polymer films.[60] However, there are substantial differences in the rate of charge decay: for all types of nanosheets, the charge decay proceeds slower for positive charges than for negative ones. For example, after 100 min at 70 °C, the positively

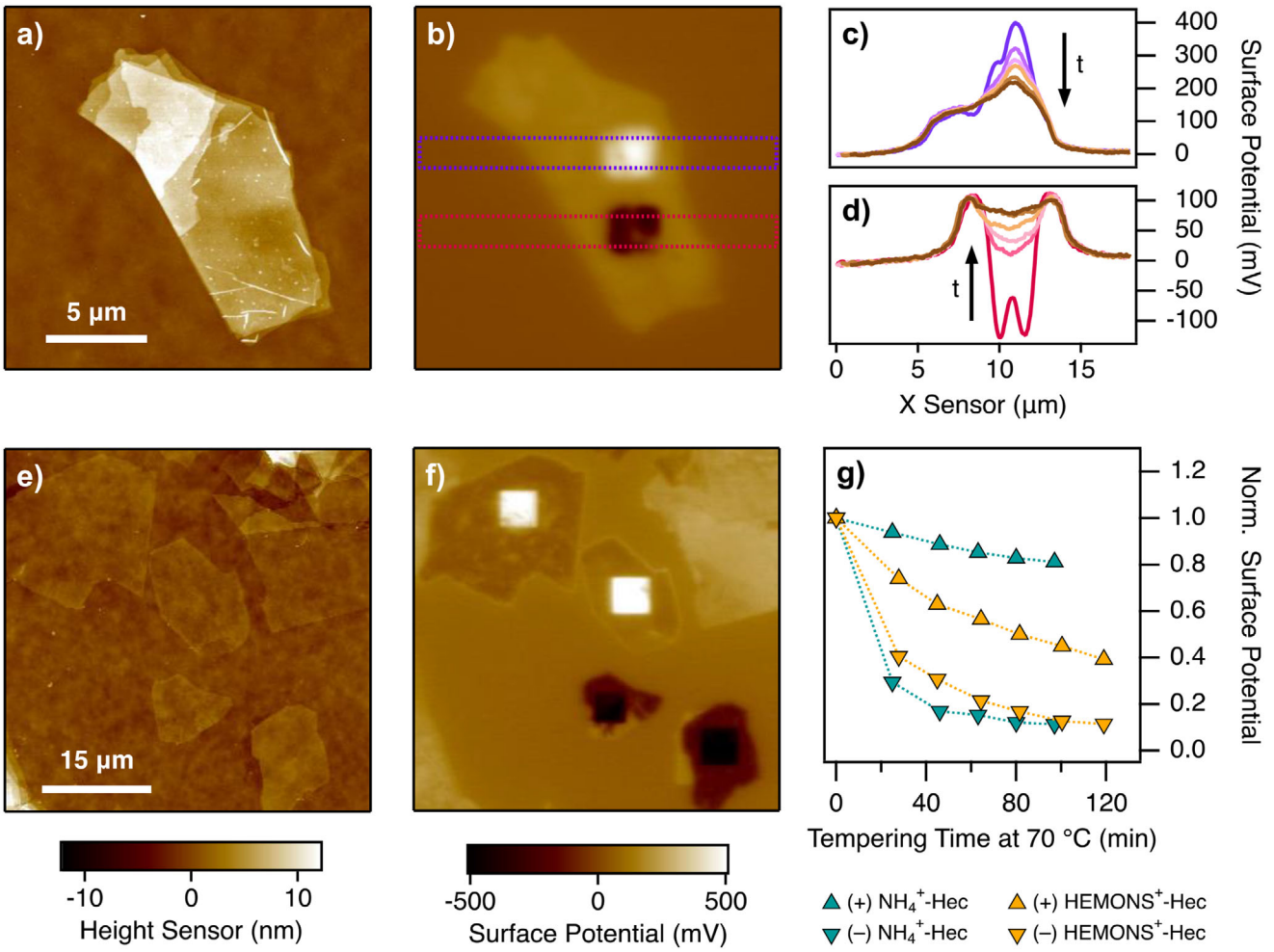

Figure 7. Surface potential decay on AFM-contact-charged double-stack materials. Typical AFM topography images after contact charging of a) HEMONS$^+$-double stacks and e) NH_4^+-double stacks. The corresponding KPFM surface potential images (b,f) show square-shaped charge patterns with positive and negative polarity. Cross-sectional analysis is indicated by dashed boxes in the potential map of the HEMONS$^+$-double stack (b). Averaged surface potential sections are shown for various times of annealing at 70 °C for c) positive charging potentials and d) negative ones. g) Normalized surface potential vs annealing time for the positive and negative charge patterns. Dotted lines are a guide to the eye.

charged areas on NH_4^+-double stacks still feature a surface potential 81 % of the initial value, whereas the remaining surface charge in the negatively charged areas is only 11 %. However, the charge decay for HEMONS$^+$-double stacks occurs much faster. In this case, the surface potential decays to 45 % on the positively charged areas and 13 % on the negative ones in the same time interval (100 min). The charge patterns on NH_4^+-double stacks show much sharper boundaries than those on HEMONS$^+$-double stacks (cf. Figure 7b,f, respectively). However, a 'smearing' out of the charge patterns during annealing was difficult to observe and quantify. Most likely, the charge decay takes place orthogonally to the platelet in the direction of the Au-electrode, as reported for organic electret films.[60] Nevertheless, the faster decay for a HEMONS$^+$ interlayer is expected from the larger dipole moment of these molecules.

By contrast, the charged structures on the Na^+-monolayer nanosheets were barely detectable (cf. Figure S7, Supporting Information) when the charge was written at +3 V, which was an upper limit due to the predetermined breakdown voltage. During annealing, an extremely fast charge decay was observed for the monolayers. At 70 °C for ≈20 min, only 10% of the initial potential was detectable. Therefore, further quantification of the isothermal annealing behavior was not possible for these nanosheets.

3. Conclusion

Clays are ubiquitous in nature and are among the most sustainable and green materials. They are not only used in the formulation of colloidal suspensions but also as fillers in composite materials. For applications in innovative insulation composites, the electrical breakdown characteristics are not only predetermined by the matrix material but also by the inorganic filler, such as the clay nanosheets used in this study. Hence, properties like the electrical treeing characteristics can be adjusted to the needs. However, in order to compile the dielectric behavior of such complex composite systems, it is important to have a quantitative understanding on the level of single nanosheets.

The scanning probe techniques used here enable such measurements for the first time. It became clear that the denser NH_4^+-double stacks provided better breakdown characteristics than the hybrid HEMONS$^+$-double stacks. While this finding is not unexpected, it is surprising that the effect is not more pronounced. Therefore, the development of functional clay materials, for example with organocations in the interlayer, will conserve in many cases the interesting dielectric properties of clays. However, by incorporating organic dyes in the interlayer, new functionality can be introduced.[51] We could demonstrate that the interlayer composition and nature provides another promising route to tune the electrical properties of the clay materials: While the charge storage of clays has practical applications[28] and the use of clay as an electret material has been reported before,[34] the role of the interlayer species has been largely omitted. The isothermal potential decay measurements clearly demonstrate that double stacks held together by an appropriate non-swelling interlayer cation lead to much better charge storage characteristics. However, the role of confined water layers,[78] especially in relation to charge storage and breakdown has to be studied further. Humidity-dependent measurements might be helpful in this respect. In the case of double-stacks, it has been observed that the process follows some steps, which would be inline with the presence of thermally induced cavities.

While some 2D dielectrics, such as MoS_2[39] or hexagonal boron nitride,[57,67] have received much attention as future building blocks for the construction of nano-electronic devices,[86–88] clay-based materials have barely been considered, although they qualify for the formation of nano-domains and charge-based self-assembly. In this respect, the interlayer will provide not only a chance to incorporate additional functionality but also to tune the dielectric properties.

4. Experimental Section

Synthesis of 6-[3-(4-Nitrostyryl)-6-methoxyphenyloxy]-hexyl triethyl Ammonium Bromide (HEMONS): Synthesis of 4-Nitro-3'-(6-bromohexyloxy)-4'-methoxystilbene (Compound **1a**): 3-Hydroxy-4-methoxy-4'-nitrostilbene (1.25 g, 4.61 mmol)[89] was dissolved in acetonitrile, K_2CO_3 (995 mg, 7.21 mmol) and 1,6-dibromohexane (3.0 mL, 19.42 mmol) were added. The reaction mixture was stirred under reflux for 7 h. The solvent was evaporated, and the residue was taken up in ethyl acetate and water. The organic phase was dried over Na_2SO_4, filtered, and concentrated in vacuum. The residue was purified by column chromatography (silica gel 60, ethyl acetate / *n*-hexane 1:3). Yield: 1.50 g (3.46 mmol, 75%); yellow solid; n_{max} (ATR)/cm^{-1}: 2935, 2857, 2837, 1625, 1586, 1509, 1474, 1462, 1431, 1397, 1341, 1263, 1242, 1230, 1212, 1164, 1136, 1107, 1023, 1008, 961, 952, 864, 850, 832, 800, 777, 746, 722, 689; ^{1}H NMR (300 MHz, $CDCl_3$): δ 1.5-1.6 (4 H, m), 1.8-2.0 (4 H, m), 3.41 (2 H, t, ^3J 6.8 Hz), 3.88 (3 H, s), 4.06 (2 H, t, ^3J 6.8 Hz), 6.86 (1 H, d, ^3J 8.8 Hz), 6.96 (1 H, d, ^3J 16.3 Hz), 7.0-7.1 (2 H, m), 7.18 (1 H, d, ^3J 16.3 Hz), 7.57 (2 H, dd, ^3J 7.0 Hz, ^4J 1.8 Hz), 8.17 (2 H, dd, ^3J 7.0 Hz, ^4J 1.8 Hz); ^{13}C NMR (75.5 MHz, $CDCl_3$): δ 25.2, 27.9, 29.0, 32.6, 33.8, 56.0, 68.9, 110.9, 111.6, 120.9, 124.1, 124.2, 126.5, 129.2, 133.2, 144.2, 146.4, 148.7; *m/z* (%) 435 (72) [M$^+$], 433 (71) [M$^+$], 271 (100), 256 (30).

Compound **1a** (780 mg, 1.80 mmol) was dissolved in acetonitrile (30 mL) and treated with Et_3N (3 mL). The reaction mixture was stirred under reflux for 16 h. The solution was cooled down to room temperature, washed twice with *n*-hexane and concentrated in vacuum. Yield: 880 mg (1.78 mmol, 99%); orange oil; n_{max} (ATR)/cm^{-1}: 2980, 2943, 2833, 1629, 1586, 1509, 1464, 1444, 1427, 1398, 1332, 1251, 1226, 1164, 1134, 1106, 1022, 952, 853, 796, 778, 748, 693; ^{1}H NMR (300 MHz, $CDCl_3$): δ 1.04 (9 H, t, ^3J 7.1 Hz), 1.1-1.3 (4 H, m), 1.4-1.6 (4 H, m), 2.9-3.1 (2 H, m), 3.15 (6 H, q, ^3J 7.1 Hz), 3.54 (3 H, s), 3.74 (2 H, t, ^3J 6.5 Hz), 6.53 (1 H, d, ^3J 8.4 Hz), 6.7-6.8 (2 H, m), 6.83 (1 H, d, ^4J 1.7 Hz), 6.90 (1 H, d, ^3J 16.3 Hz), 7.31 (2 H, d, ^3J 8.9 Hz), 7.80 (2 H, d, ^3J 8.9 Hz); ^{13}C NMR (75.5 MHz, $CDCl_3$): δ 7.2, 21.1, 24.7, 25.3, 28.1, 45.6, 52.6, 55.2, 56.6, 67.9, 110.4, 110.9, 120.3, 123.1, 123.4, 125.9, 128.5, 132.4, 143.6, 145.3, 147.8, 149.5; *m/z* (%) 413 (42) [M$^+$], 353 (18), 271 (100), 256 (21), 86 (73).

Synthesis of Hectorites: Sodium fluorohectorite ($Na_{0.5}{}^{inter}[Mg_{2.5}Li_{0.5}]^{oct}<Si_4>^{tet}O_{10}F_2$) was prepared by melt synthesis in a closed molybdenum crucible according to a well-established procedure.[90,91] To improve the charge homogeneity, intracrystalline reactivity, and phase purity, the raw material was annealed for six weeks at 1045 °C.[46] The material featured a cation exchange capacity (CEC) of 1.27 mmol/g and a density of 2.73 g cm^{-3}.

Synthesis of Ordered Heterostructures with Alternating Na^+/ NH_4^+ Interlayers: The production of hectorite double stacks with specific interlayer cations was achieved by first synthesizing ordered interstratifications of the layered silicate and subsequent delamination in pure water.[64,92] First, 1.5 g of Na^+-hectorite was immersed in 250 mL of a water-ethanol mixture (75 vol% ethanol) for 12 h at room temperature in an overhead shaker. Then, 70.3 mg of NH_4Cl (Grüssing GmbH, Germany), corresponding to 69% of the CEC of Na^+-hectorite,[50] was dissolved in 100 mL of a water-ethanol mixture (75 vol% ethanol) and added to the Na^+-hectorite under vigorous stirring followed by equilibration in the overhead shaker overnight at room temperature. The heterostructure was then washed five times with the same ethanol-water mixture and collected via centrifugation at 8000 rpm for 10 min. The ordered heterostructure was indicated by a rational superstructure *00l* series with a basal spacing of 23.0 Å. at 43% relative humidity. When immersed in deionized water, the heterostructure delaminates spontaneously into NH_4^+-double stacks and a birefringent gel was formed.

Preparation of Hectorite Bilayers with Alternating Na^+ / HEMONS$^+$ Interlayers: Interstratified samples were prepared in centrifuge tubes sealed with a septum in Argon atmosphere. Mixing at 40 °C was performed using a temperature-controlled oven equipped with a self-made overhead shaker. During the preparation of the intercalated compounds, the amount of solvent was adjusted concomitantly with the variation of the complex amount to keep the complex concentration for all samples constant at 1 mmol dm^{-3}.

For instance, Na^+-hectorite hydrated at 43% relative humidity (10.73 mg) was pre-dispersed in 75 vol% acetonitrile (2.12 cm^3) for 30 min at room temperature using an overhead shaker. With 75% acetonitrile as the dispersing solvent, the interlayer space was widened by crystalline swelling to 2 nm, which greatly facilitates the intercalation kinetics of the bulky organocation.[93] After adding a HEMONS$^+$ solution in 75% acetonitrile (1 mmol dm^{-3}) in an amount corresponding to 45% of the cation exchange capacity (CEC) of the pristine Na^+-hectorite, the dispersion was mixed at 80 °C and equilibrated for 24 h to assure ordered heterostructures.[49] Please note that ordered interstratifications require equal weighting of the two types of interlayers. As the organization interlayer in the dense packing happens to have a charge density lower than the charge density of the clay host, in this case less than 50% of the CEC was required.[94] The solid was separated four-fold by sedimentation followed by centrifugation at 1270 ×g for 5 min and washing with 75 vol% aqueous acetonitrile to remove the remaining salts. Finally, water was added to the 75 vol% acetonitrile suspension in a dropwise manner up to the point where the concentration of acetonitrile was decreased to 25 vol%. Decreasing the concentration of acetonitrile below 50% triggers the spontaneous delamination of the heterostructures into double stacks.[47] Finally, the acetonitrile was completely removed by thorough washing with demineralized water followed by centrifugation at 14090 ×g (Heraeus Multifuge) and redispersion in water.

Sample Preparation: Template-stripped Au substrates were prepared on 11 × 11 mm^2 glass slides using a procedure described elsewhere.[61,62] First, freshly cleaved template-stripped gold substrates were plasma treated for 30 s at a power of 100 W in a Diener Zepto (Diener electronic,

Germany) plasma cleaner. Then, 200 µL of 1 mg mL^{-1} aqueous solutions of delaminated hectorite nanosheets (double stacks with non-swelling interlayer cations or monolayers) were instantly placed onto the plasma-treated Au substrates. After 1 h, the hectorite solution was removed, and the sample was dried at room temperature overnight. This procedure resulted in delaminated hectorite nanosheets on the surface. However, also bi- and trilayers could be found for all interlayer types, albeit to a much lower extend.

To implement an electrical connection of the Au substrate, a polyimide-insulated silver wire (0.125 mm diameter, Advent Research Materials, England) was fixed at the Au-layer rim using the conductive silver paint ACHESON 1415 purchased from Plano, Germany.

Nanoelectrical Breakdown Measurements: All AFM measurements were performed on a Dimension ICON AFM equipped with a Nanoscope V controller (Bruker, USA). The AFM was set up in an acoustic isolation enclosure, which also prevents the deposition of contaminations onto the charged platelets. Samples were placed on the AFM stage, and the Au layer of the substrate was connected to the AFM controller ground using the silver wire mentioned above.

For conductive AFM measurements and I–V ramping, the PeakForce TUNA Nanoelectrical application module (Bruker, USA) was used. Full platinum wire cantilevers (RMN-25PT300B, Rocky Mountain Nanotechnology, USA) with a nominal resonance frequency of 20 kHz and a spring constant of 18 N m^{-1} were used. The topography and current images were acquired simultaneously using the contact mode in air. The imaging parameters were adjusted under consideration of the respective platelet dimensions. During image acquisition, a small DC voltage was applied to the Au substrate. I–V curves were acquired on individual platelets by ramping the sample potential from 0 to 10 V or 0 to −10 V and back, respectively. The applied force was gradually increased until stable I–V curves were measured on the Au substrate (typically in an estimated range of 350–650 nN). After recording an I–V curve on a silicate platelet, one subsequent voltage ramp in the range of −1 to +1 V was conducted on a single spot of the bare gold substrate in order to verify an ohmic contact with a linear I–V curve and thereby to rule out contamination of the tip. If deviations from the linear behavior occurred, the contaminated tips were cleaned by dipping the probes several times in ethanol (p.a.) and pure water. In case of persistent contamination, the cantilevers were additionally plasma-treated for 5 min.

Controlled Charging and Isothermal Potential Decay Measurements on Hectorite Nanosheets: For the ensuing experiments, the same AFM device was used. Samples were placed and grounded on a Bruker heater chuck connected to a LakeShore 335 temperature controller (Lake Shore Cryotronics, USA) to allow for charge decay experiments at elevated temperatures.

AFM's optical microscopy was used for coarse navigation on the sample and captured a preliminary topographical image for identifying a hectorite nanosheet that was suitable for the charging experiments. The defined charge patterning was achieved by using the AFM's nanolithography interface NanoMan (Bruker, USA). After contact charging, the created patterns were read-out via a dual-pass amplitude modulation KPFM (30 nm lift height). For this purpose, platinum/iridium-coated, conductive SCM-PIT-V2 cantilevers (Bruker, USA) with a nominal resonance frequency of 75 kHz and a nominal spring constant of 2.8 N m^{-1} were used.

For the surface potential decay investigations, charged areas were created using the contact mode in air with a setpoint of 25–50 nN and a tip velocity between (2.0–5.0) µm s^{-1} depending on the charged area. A positive or negative potential of ± 3 V was applied to the cantilever during scanning. Dual-pass amplitude modulation KPFM measurements in air were performed directly after contact charging using the same measurement setup. The sample topography was recorded in the tapping mode, whereas the surface potential was acquired at a lift height of 50 nm. After the first KPFM scan at room temperature, the sample was in situ tempered at 70 °C, and consecutive KPFM scans were performed.

Image processing, data analysis, and visualization were performed with NanoScope Analysis v1.50 and Igor Pro (WaveMetrics, Inc., USA).

Supporting Information

Supporting Information is available from the Wiley Online Library or from the author.

Acknowledgements

S.G. and P.M. contributed equally to this work. The authors acknowledge financial support by the German Research Foundation (DFG) (Project number 492723217 (CRC 1585), subproject A05) for financial support and Florian Puchtler for the synthesis of the clay. P.M. acknowledges the support by the Elite Network of Bavaria (ENB) through the study program "Macromolecular Science." The authors thank Professor Sallaberger from the Department of Cultural Studies and Classical Studies at the University of Munich for his valuable input concerning the cuneiform text.

Open access funding enabled and organized by Projekt DEAL.

Conflict of Interest

The authors declare no conflict of interest.

Data Availability Statement

The data that support the findings of this study are available from the corresponding author upon reasonable request.

Keywords

2D electronics, conductive AFM, dielectric breakdown, dielectric charging, isothermal potential decay, Kelvin probe force microscopy, layered silicates

Received: April 10, 2025
Revised: May 11, 2025
Published online: July 11, 2025

[1] D. D. Eisenhour, R. K. Brown, *Elements* **2009**, *5*, 83.
[2] G. Lagaly, S. Ziesmer, *Adv. Colloid Interface Sci.* **2003**, *100*, 105.
[3] K. Radner, E. Robson, *The Oxford Handbook of Cuneiform Culture*, Oxford University Press, Oxford, NY **2011**.
[4] M. Röhrl, R. L. Timmins, S. Rosenfeldt, D. D. Schuchardt, F. Uhlig, S. Nürmberger, J. Breu, *ACS Appl. Mater. Interfaces* **2023**, *15*, 22524.
[5] Q. L. Zhu, C. F. Dai, D. Wagner, O. Khoruzhenko, W. Hong, J. Breu, Q. Zheng, Z. L. Wu, *Adv. Sci.* **2021**, *8*, 2102353.
[6] C. Habel, E. S. Tsurko, R. L. Timmins, J. Hutschreuther, R. Kunz, D. D. Schuchardt, S. Rosenfeldt, V. Altstädt, J. Breu, *ACS Nano* **2020**, *14*, 7018.
[7] A. Teepakakorn, M. Ogawa, *Appl. Clay Sci.* **2022**, *222*, 106487.
[8] T. Dörres, M. Bartkiewicz, K. Herrmann, M. Schöttle, D. Wagner, Z. Wang, O. Ikkala, M. Retsch, G. Fytas, J. Breu, *ACS Appl. Nano Mater.* **2022**, *5*, 4119.
[9] N. Sakhavand, R. Shahsavari, *Nat. Commun.* **2015**, *6*, 6523.
[10] Y. Cui, S. Kumar, B. Rao Kona, D. van Houcke, *RSC Advances* **2015**, *5*, 63669.
[11] A. Idris, A. Muntean, B. Mesic, *J. Coat. Technol. Res.* **2022**, *19*, 699.
[12] M. W. Möller, T. Lunkenbein, H. Kalo, M. Schieder, D. A. Kunz, J. Breu, *Adv. Mat.* **2010**, *22*, 5245.
[13] D. J. Chen, R. W. Staley, 1967 *Seventh Electrical Insulation Conference*, IEEE, Chicago, IL, USA **1967**.
[14] R. L. Griffeth, E. R. Younglove, *Electr. Eng.* **1952**, *71*, 463.

[15] M. Ghassemi, *High Voltage* **2020**, *5*, 7.
[16] M. G. Danikas, T. Tanaka, *IEEE Electr. Insul. Mag.* **2009**, *25*, 19.
[17] R. Vogelsang, T. Farr, K. Frohlich, *IEEE Trans. Dielectr. Electr. Insul.* **2006**, *13*, 373.
[18] B. Pacakova, P. E. Vullum, A. Kirch, J. Breu, C. R. Miranda, J. O. Fossum, *MRS Bull.* **2022**, *47*, 1198.
[19] F. Zeng, X. Chen, G. Xiao, H. Li, S. Xia, J. Wang, *ACS Nano* **2020**, *14*, 611.
[20] I. I. Inculet, R. M. Quigley, *J. Electrostat.* **1989**, *24*, 61.
[21] G. K. Novikov, V. V. Fedchishin, *Russ. Phys. J.* **2015**, *57*, 1642.
[22] M. G. Broadhurst, G. T. Davis, *Topics in Applied Physics: Electrets*, Springer, Berlin Heidelberg **1987**.
[23] K. C. Kao, *Dielectric Phenomena in Solids*, Academic Press, San Diego California USA **2004**.
[24] R. Kressmann, G. M. Sessler, P. Gunther, *IEEE Trans. Dielectr. Electr. Insul.* **1996**, *3*, 607.
[25] X. Zhang, Y. He, R. Li, H. Dong, W. Hu, *Adv. Mat.* **2016**, *28*, 3755.
[26] Y. Bitla, Y.-H. Chu, *FlatChem* **2017**, *3*, 26.
[27] C. Wei, A. Roy, M. Tripathi, A. K. A. Aljarid, J. P. Salvage, S. M. Roe, R. Arenal, C. S. Boland, *Adv. Mat.* **2023**, *35*, 2303570
[28] M. N. V. McDougall, R. P. N. Veregin, G. G. Sacripante, V. M. Farrugia, European Patent Office EP 2026134 B1 (Xerox), **2013**.
[29] M. Tomita, S. Emoto, H. Yamasita, T. Sugiyama, European Patent Office EP1293839 B1 (Ricoh), **2009**.
[30] R. P. N. Veregin, D. W. Vanbesien, C. Vong, US Patent Office 007759039 B2 (Xerox), **2010**.
[31] S. K. Ghosh, W. Rahman, T. R. Middya, S. Sen, D. Mandal, *Nanotechnology* **2016**, *27*, 215401.
[32] W. Rahman, S. K. Ghosh, T. R. Middya, D. Mandal, *AIP Conf. Proc.* **2018**, *1942*, 050081.
[33] T. Rodrigues-Marinho, N. Perinka, P. Costa, S. Lanceros-Mendez, *Mater. Today Sustain.* **2023**, *21*, 100292.
[34] K. Wang, Y. Zhang, X. Luo, L. Zhu, Z. L. Wang, *ACS Appl Electr. Mat.* **2022**, *4*, 4764.
[35] M. F. Frechette, M. L. Trudeau, H. D. Alamdari, S. Boily, *IEEE Trans. Dielectr. Electr. Insul.* **2004**, *11*, 808.
[36] H. Goronkin, Y. Yang, *MRS Bull.* **2004**, *29*, 805.
[37] B. J. Park, J. H. Sung, J. H. Park, J. S. Choi, H. J. Choi, *J. Nanosci. Nanotechnol.* **2008**, *8*, 2676.
[38] J. Zhu, X. Liu, M. L. Geier, J. J. McMorrow, D. Jariwala, M. E. Beck, W. Huang, T. J. Marks, M. C. Hersam, *Adv. Mat.* **2016**, *28*, 63.
[39] L. Li, M. Wu, *ACS Nano* **2017**, *11*, 6382.
[40] P. L. Mahapatra, G. Costin, D. S. Galvao, B. Lahiri, N. Glavin, A. K. Roy, P. M. Ajayan, C. S. Tiwary, *2D Mater.* **2024**, *11*, 032003.
[41] D. A. Kunz, J. Erath, D. Kluge, H. Thurn, B. Putz, A. Fery, J. Breu, *ACS Appl. Mater. Interfaces* **2013**, *5*, 5851.
[42] V. Kuznetsov, K. Ottermann, N. Helfricht, D. Kunz, P. Loch, H. Kalo, J. Breu, G. Papastavrou, *Colloid Polym. Sci.* **2020**, *298*, 907.
[43] A. Maruvada, K. Shubhakar, N. Raghavan, K. L. Pey, S. J. O'Shea, *Sci. Rep.* **2022**, *12*, 14076.
[44] A. Maruvada, S. J. O'Shea, J. Deng, S. Kalya, N. Raghavan, K. L. Pey, 2023 IEEE Nanotechnology Materials and Devices Conference (NMDC), IEEE, Paestum, Italy **2023**, 452.
[45] A. Maruvada, S. J. O'Shea, J. Deng, K. Shubhakar, N. Raghavan, K. L. Pey, *Appl. Phys. Lett.* **2024**, *125*, 112904.
[46] M. Stöter, D. A. Kunz, M. Schmidt, D. Hirsemann, H. Kalo, B. Putz, J. Senker, J. Breu, *Langmuir* **2013**, *29*, 1280.
[47] M. Stöter, S. Rosenfeldt, J. Breu, *Annu. Rev. Mater. Res.* **2015**, *45*, 129.
[48] V. Dudko, O. Khoruzhenko, S. Weiß, M. Daab, P. Loch, W. Schwieger, J. Breu, *Adv. Mater. Technol.* **2023**, *8*, 2200553.
[49] M. Stöter, B. Biersack, N. Reimer, M. Herling, N. Stock, R. Schobert, J. Breu, *Chem. Mater.* **2014**, *26*, 5412.
[50] M. Stöter, S. Gödrich, P. Feicht, S. Rosenfeldt, H. Thurn, J. W. Neubauer, M. Seuss, P. Lindner, H. Kalo, M. Möller, A. Fery, S. Förster, G. Papastavrou, J. Breu, *Angew. Chem.* **2016**, *55*, 7398.
[51] C. Schnupfhagn, T. Schumacher, P. Markus, G. Papastavrou, O. Aftenieva, T. A. F. König, V. Dudko, M. Matejdes, J. Breu, M. Lippitz, *Nano Lett.* **2022**, *22*, 7499.
[52] F. Palumbo, C. Wen, S. Lombardo, S. Pazos, F. Aguirre, M. Eizenberg, F. Hui, M. Lanza, *Adv. Func. Mat.* **2020**, *30*, 1900657.
[53] P. F. Pieters, A. Lainé, H. Li, Y.-H. Lu, Y. Singh, L.-W. Wang, Y. Liu, T. Xu, A. P. Alivisatos, M. Salmeron, *ACS Nano* **2022**, *16*, 6744.
[54] C. M. Osburn, D. W. Ormond, *J. Electrochem. Soc.* **1972**, *119*, 591.
[55] M. Porti, M. Nafrıá, X. Aymerich, A. Olbrich, B. Ebersberger, *J. Appl. Phys.* **2002**, *91*, 2071.
[56] H. Watanabe, T. Baba, M. Ichikawa, *J. Appl. Phys.* **1999**, *85*, 6704.
[57] L. Britnell, R. V. Gorbachev, R. Jalil, B. D. Belle, F. Schedin, M. I. Katsnelson, L. Eaves, S. V. Morozov, A. S. Mayorov, N. M. R. Peres, A. H. Castro Neto, J. Leist, A. K. Geim, L. A. Ponomarenko, K. S. Novoselov, *Nano Lett.* **2012**, *12*, 1707.
[58] A. Ranjan, N. Raghavan, M. Holwill, K. Watanabe, T. Taniguchi, K. S. Novoselov, K. L. Pey, S. J. O'Shea, *ACS Appl. Electron. Mater.* **2021**, *3*, 3547.
[59] C. Li, S. Minne, B. Pittenger, A. Mednick, M. Guide, T. Q. Nguyen, Simultaneous electrical and mechanical property mapping at the nanoscale with the PeakForce TUNA, Bruker Application Note AN132 Rev. A, **2011**, https://www.bruker.com/de/products-and-solutions/microscopes/materials-afm/resource-library/an-132-simultaneous-electrical-and-mechanical-property-mapping-at-the-nanoscale-with-peakforce-tuna.html.
[60] S. Gödrich, H.-W. Schmidt, G. Papastavrou, *ACS Appl. Mater. Interfaces* **2022**, *14*, 4500.
[61] M. Hegner, P. Wagner, G. Semenza, *Surf. Sci.* **1993**, *291*, 39.
[62] V. Kuznetsov, G. Papastavrou, *Langmuir* **2012**, *28*, 16567.
[63] H. Kalo, W. Milius, J. Breu, *RSC Adv.* **2012**, *2*, 8452.
[64] M. Stöter, B. Biersack, S. Rosenfeldt, M. J. Leitl, H. Kalo, R. Schobert, H. Yersin, G. A. Ozin, S. Förster, J. Breu, *Angew. Chem.* **2015**, *54*, 4963.
[65] Y. Zhang, Y. Miyahara, N. Derriche, W. Yang, K. Yazda, X. Capaldi, Z. Liu, P. Grutter, W. Reisner, *Small Methods* **2019**, *3*, 1900147.
[66] K. C. Kao, *J. Appl. Phys.* **1984**, *55*, 752.
[67] Y. Hattori, T. Taniguchi, K. Watanabe, K. Nagashio, *ACS Nano* **2015**, *9*, 916.
[68] DIN EN 60243-1 (VDE 0303–21) Electric Strenght of Insulation Materials – Test Methods, VDE Verlag, Berlin & Offenbach **2014**.
[69] Advancing Standards Transforming Markets International, *Standard Test Method for Dielectric Breakdown Voltage and Dielectric Strength of Solid Electrical Insulating Materials at Commercial Power*, Advancing Standards Transforming Markets International, West Conshohocken, PA **2020**.
[70] H. C. Lin, P. D. Ye, G. D. Wilk, *Appl. Phys. Lett.* **2005**, *87*, 182904.
[71] H. Fröhlich, N. F. Mott, *Proc. R. Soc. Lond. A Math. Phys. Sci.* **1939**, *171*, 496.
[72] A. E. W. Austen, S. Whitehead, *Proc. R. Soc. Lond. A Math. Phys. Sci.* **1940**, *176*, 33.
[73] A. T. Davidson, A. D. Yoffe, *Nature* **1965**, *206*, 1247.
[74] H. Fröhlich, *Proc. R. Soc. Lond. A Math. Phys. Sci.* **1941**, *178*, 493.
[75] R. Haag, M. A. Rampi, R. E. Holmlin, G. M. Whitesides, *J. Am. Chem. Soc.* **1999**, *121*, 7895.
[76] D. J. Wold, C. D. Frisbie, *J. Am. Chem. Soc.* **2001**, *123*, 5549.
[77] C. A. Peterson, R. K. Workman, D. Sarid, B. Vermeire, H. G. Parks, D. Adderton, P. Maivald, *J. Vac. Sci. Technol. A: Vac. Surf. Films* **1999**, *17*, 2753.
[78] Q. Li, J. Song, F. Besenbacher, M. Dong, *Acc. Chem. Res.* **2015**, *48*, 119.
[79] G. Yan, M. Zhang, Z. Sun, P. Zhao, B. Zhang, *Miner. Eng.* **2024**, *205*, 108478.
[80] L. Collins, J. I. Kilpatrick, S. V. Kalinin, B. J. Rodriguez, *Rep. Prog. Phys.* **2018**, *81*, 086101.
[81] E. Rani, L. S. Wong, *Adv. Mater. Technol.* **2019**, *4*, 1900181.

[82] Y. S. Zhou, Y. Liu, G. Zhu, Z.-H. Lin, C. Pan, Q. Jing, Z. L. Wang, *Nano Lett.* **2013**, *13*, 2771.
[83] C. Mittermayer, *Altbabylonische Zeichenliste der sumerisch-literarischen Texte*, Presses Universitaires Fribourg, Fribourg, Switzerland **2006**.
[84] P. Fan, J. Gao, H. Mao, Y. Geng, Y. Yan, Y. Wang, S. Goel, X. Luo, *Micromachines* **2022**, *13*, 228.
[85] N. Knorr, S. Vinzelberg, *Microsc. Microanal.* **2012**, *26*, 7.
[86] A. Lipatov, T. Li, N. S. Vorobeva, A. Sinitskii, A. Gruverman, *Nano Lett.* **2019**, *19*, 3194.
[87] A. Lipatov, P. Chaudhary, Z. Guan, H. Lu, G. Li, O. Crégut, K. D. Dorkenoo, R. Proksch, S. Cherifi-Hertel, D.-F. Shao, E. Y. Tsymbal, J. Íñiguez, A. Sinitskii, A. Gruverman, *NPJ 2D Mater. Appl.* **2022**, *6*, 18.
[88] U. Zaghloul, B. Bhushan, G. Papaioannou, F. Coccetti, P. Pons, R. Plana, *J. Colloid Interface Sci.* **2012**, *365*, 236.
[89] Z. Li, K. Wu, G. Su, Y. He, *Opt. Mater.* **2002**, *20*, 295.
[90] J. Breu, W. Seidl, A. J. Stoll, K. G. Lange, T. U. Probst, *Chem. Mater.* **2001**, *13*, 4213.
[91] H. Kalo, M. W. Möller, D. A. Kunz, J. Breu, *Nanoscale* **2012**, *4*, 5633.
[92] O. Khoruzhenko, V. Dudko, S. Rosenfeldt, J. Breu, *Mater. Horiz.* **2023**, *10*, 3749.
[93] R. Kunz, S. Amschler, A. Edenharter, L. Mayr, S. Herlitz, S. Rosenfeldt, J. Breu, *Clays Clay Miner.* **2019**, *67*, 481.
[94] M. Matejdes, M. Stöter, R. Czerwieniec, M. Leitl, S. Rosenfeldt, T. Schumacher, J. Albert, M. Lippitz, H. Yersin, J. Breu, *Adv. Opt. Mater.* **2021**, *9*, 2100516.